Active Two-Way Backscatter Modulation: An Analytical Study

Seiran Khaledian, *Student Member, IEEE,* Farhad Farzami, *Student Member, IEEE,* Hamza Soury, *Member, IEEE,* Besma Smida, *Senior Member, IEEE,* and Danilo Erricolo, *Fellow, IEEE*

***Abstract*—Backscatter modulation (BM), usually used for Radio Frequency Identifications (RFID), has the potential to be exploited in wider range of applications such as Internet of Things and wireless sensor networks. In this paper, we leverage BM by increasing its down-link (from reader to tag) and up-link (from tag to reader) range. We propose two active two-way BM tag configurations, named parallel and series. For both configurations, we use active loads in the tag modulators to maximize the BM range and implement the desired backscattered constellation, subject to no data loss in down-link path. Contrary to most existing BM studies, we use Thevenin/Norton equivalent circuit, *only* to calculate the received power at tag, while we derive the tag backscattered power using the antenna scatterer theorem. Moreover, we obtain a closed-form expression of the average bit error probability (BEP) at reader in Rician fading channel environment for both tag configurations. We compare the proposed active BM tags with the conventional passive BM tag. The simulation results prove that for an average BEP equals to 10^{-4}, an SNR improvement of up to 19 dB and 24 dB can be achieved for parallel and series configurations, respectively.**

***Index Terms*—Backscatter modulation, performance evaluation, negative resistance, reflection amplifier, bidirectional amplifier, read-write backscatter tag, RFID tags, IoT, geometric representation.**

I. Introduction

THE history of backscatter modulation (BM) traces back to the foundational paper of Stocksman in 1948 [1]. Stockman proposed a point-to-point communication, with the carrier power generated at the reader and reflected back by a modulating reflector at the BM tag. BM is based on the reflection of electromagnetic waves. BM takes advantage of the presence of reflection coefficient variations at the interface between the tag antenna and its input load. By varying the BM tag loads (Z_1 to Z_n), the reflection coefficient changes and the reflected signal is modulated, as illustrated in Fig. 1.

This setup is capable of modulating data upon the original waveform, which can be received and decoded. The BM tag does not need to actively transmit any radio signal. This leads to very low-cost implementations at the BM tag. Thus, BM has found many applications among which Radio Frequency Identifications (RFIDs) are the most prominent. Over the last three decades, a great deal of effort has been focused on using BM in manufacturing RFID tags with passive loads and on/off keying (OOK) BM constellation to identify objects,

The authors are with Department of Electrical and Computer Engineering, University of Illinois at Chicago, Chicago, IL 60607 USA. Emails: {skhale6, ffarza2, soury, smida, derric1}@uic.edu. This work was partially funded by the National Science Foundation CAREER award #1620902. We would like to thank Dr. Daniel P. Bailey from University of Illinois at Chicago, College of Engineering for editing of this manuscript.

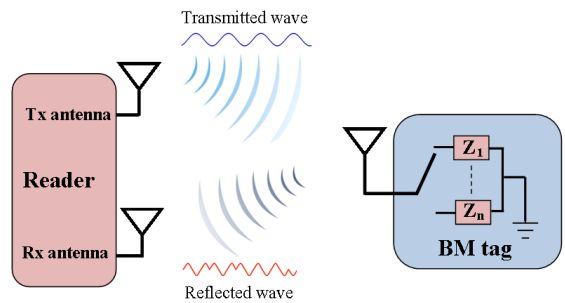

Fig. 1: Backscatter modulation illustration.

which we call conventional RFIDs. However today, with the growth of the global distributed network, known as the Internet of Things (IoT), BM tags have potential to serve not only in mere identification, but also as two-way communication nodes, to write data back onto the multiple types of devices comprising the IoT [2]. BM tags can also be integrated with sensor nodes, which makes them capable of even a larger variety of applications including both industrial [3] and medical [4]. Recently, BM has been proposed for use in full-duplex wireless communication systems in our previous research [5]–[7]. In these studies, a full-duplex communication system by means of BM is proposed to avoid self-interference signal at end-user and the final throughput is derived to prove that its performance is competitive compared to conventional full-duplex system.

Here, we intend to exploit BM in two-way wireless communication systems such as IoT circuits, full-duplex communication and wireless sensor networks. In contrast to the approach of passive and conventional one-way RFID tags, we do not use BM to take advantage of its low-power requirements. Instead, we employ active BM to allow the transmission of two-way flows of data over the same carrier at the same time, with improved communication range. Accordingly, we need to overcome one-way and short-range communication limitation associated with conventional BM tags due to the associated two-way path loss. Recently, several prototypes of BM tags succeeded to increase the backscatter communication range by using reflection amplifier that amplifies the reflected signal [8]–[11]. Recent researches also proposed to use appropriate signal processing, system design and multiple antennas for passive backscatter communications to extend the communication ranges, [12]–[16]. These techniques can be added to active tags to further improve the range. In a two-way BM tag,

demodulation and modulation are implemented at down-link (from reader to BM tag) and up-link (from BM tag to reader), respectively. Thus, we need to optimize the BM tag modulation loads to provide sufficient power for the tag demodulator while exhibiting maximal difference in the backscattered field. In [17], [18] an analytical study has been carried out to optimize the value of loads in a passive RFID tag to yield a four quadrature amplitude modulation (4-QAM) BM constellation, maximize the available power in the tag and achieve a bit error rate (BER) that is no greater than a predetermined threshold value.

In our paper, we propose two BM tag configurations with active loads that implement two-way wireless communications. In order to have no data loss in the down-link path, we set an additional requirement to the BM tag configurations design. The received power at the BM tag demodualtors should be at least equal to P_{match}, which is the amount of power delivered to a conventional receiver demodulator when its load is conjugate-matched to its antenna impedance. The proposed BM tag configurations, which we name parallel and series configurations, are analytically studied. By optimizing the set of modulator loads that correspond to BM constellation symbols, we a) maximize the BM communication range, b) implement the desired BM constellation map such as QAM and phase shift keying (PSK) at up-link, and c) guarantee at least P_{match} at the BM tag demodulator. We propose a new geometric representation for the optimization problem. Compared to passive RFID tags, the proposed configurations not only increase the communication range, but also enable a two-way communication. The proposed configurations use BM to avoid a separate transmitter (like active point to point tags or ZigBee modules) and decrease cost, complexity and power consumption considerably.

For the parallel BM tag configuration, we use negative resistance as the modulator load in parallel with the BM tag demodulator. The negative resistance implementation process has been thoroughly covered in [7], [19]–[21]. BM communication is realized by switching among different values of negative resistors. We use the Norton equivalent circuit (NEC) of the BM tag and the antenna scatterer theorem (AST) to derive the received and backscattered power at the BM tag, respectively. By using the proposed geometric representation of backscattered symbols, we can set the desired BM constellation map, minimize the average bit error probability (BEP) at the reader and have at least P_{match} delivered to the BM tag demodulator in an oscillation-free condition.

For the series BM tag configuration, we use a bidirectional amplifier, an impedance matching circuit (IMC_t) and a digital phase shifter in series with the BM tag demodulator. The bidirectional amplifier simultaneously amplifies both received and backscattered signals at the BM tag. Different types of bidirectional amplifiers have been proposed in the literature and their implementation processes have been covered, [19], [20], [22], [23]. By switching among different IMC_ts, bidirectional amplifier gain and phase shifter values, the desired BM constellation map is achieved. We use the Thevenin equivalent circuit (TEC) of the BM tag and the AST to derive the received and backscattered power at the BM tag, respectively.

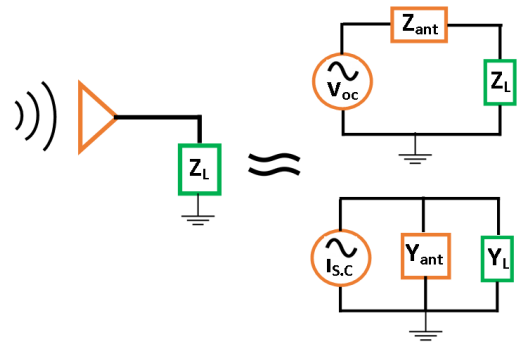

Fig. 2: TEC and NEC of a receiving antenna.

Like the parallel configuration, we use the proposed geometric representation of backscattered symbols to set the desired BM constellation map, minimize the average BEP at the reader and have at least P_{match} delivered to the BM tag demodulator in an oscillation-free condition. As an example, we also implement a 4-QAM constellation to meet all the mentioned optimization criteria for both parallel and series tag configurations.

To conclude this study, we derive a closed-form expression of the average BEP at reader in a Rician fading channel environment for both tag configurations. The simulation results show that the series tag configuration provides better average BEP at the reader, at the expense of demanding more complex circuit elements with larger size and higher power consumption.

Notations: For the rest of this paper, we specify the parameters of parallel configuration with superscript *p* and series configuration with superscript *s*. We also use superscript *n* to specify the parameters associated to each loads value in the parallel configuration. Re$(\cdot)$ and Im$(\cdot)$ denote the real and imaginary parts of the given parameter, respectively, while x^* denotes the conjugate of the complex number x and j is the imaginary unit i.e. $j^2 = -1$.

II. Receiving and Scattering Properties of Antenna

To derive the received power at the tag antenna, we use the TEC (NEC) to model the receiving antenna by a voltage source and its series impedance (current source and its shunt admittance). In this case, the voltage source is the voltage induced on the antenna at its feed point when it is an open-circuit (V_{OC}), the source impedance is the antenna input impedance (Z_{ant}) and the load impedance is the impedance of the receiver connected to the antenna (Z_L). The current source ($I_{S.C}$) is the current induced on antenna port when it is a short circuit, Y_{ant} is the antenna input admittance and Y_L is the receiver admittance, as all shown in Fig. 2. There are number of articles, comments and responses to comments trying to answer the question of how much power is scattered by a receiving antenna [24]–[26]. Contrary to the prevailing practice, the TEC/NEC can only be used to describe the current at the load and cannot be relied upon for calculating the scattered power. Instead the AST equation should be used to derive the backscattered power at the tag antenna interface [27]. Therefore, in contrast to common practice [17], [28], we

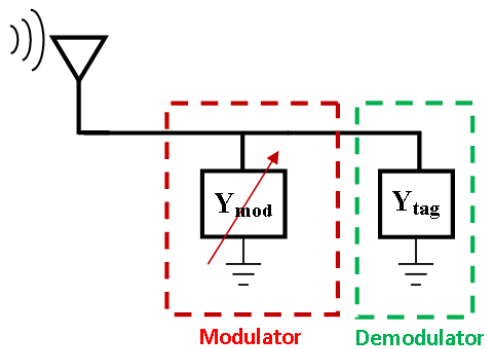

Fig. 3: Proposed parallel BM tag configuration schematic.

use AST rather than TEC/NEC to correctly evaluate the tag backscattered power. We use the AST, to derive the scattered electric field $E_{scat}(r,\theta,\phi|Z_L)$ of an antenna in free space at point (r,θ,ϕ), loaded with impedance Z_L, as [27],

$$E_{scat}(r,\theta,\phi|Z_L) = \overbrace{E_{scat}(r,\theta,\phi|Z^*_{ant})}^{\text{structure-dependent}} - \overbrace{\Gamma_L I(Z^*_{ant})\underline{E}_r(r,\theta,\phi)}^{\text{load-dependent}}, \quad (1)$$

where $E_{scat}(r,\theta,\phi|Z^*_{ant})$ is the same field as the scattered electric field when the antenna is conjugate-matched (i.e. $Z_L = Z^*_{ant}$), Z_{ant} is the antenna input impedance, $\Gamma_L = (Z_L - Z^*_{ant})/(Z_L + Z_{ant})$ is the conjugate matched reflection coefficient at antenna interface, $I(Z^*_{ant})$ is the current flowing in the antenna when the antenna is conjugate-matched, and $\underline{E}_r(r,\theta,\phi)$ is the electric field generated by the antenna as a radiator when excited by a unit current source.

III. BM Tag Parallel Configuration

In this section, we introduce the parallel configuration. We first present the BM tag structure and then derive the received and backscattered power expressions. Based on the geometric representation of the backscattered symbols, we optimize the BM tag modulator loads to implement the desired BM constellation map while maximizing the backscattered power and guaranteeing at least P_{match} at the demodulator. We also consider an oscillation-free condition in the BM tag design.

A. Parallel configuration schematic

The proposed parallel BM tag configuration includes three parts: *i*) the antenna, *ii*) the modulator loads (Y_{mod}), and *iii*) the BM tag demodulator (Y_{tag}), as shown in Fig. 3. Y_{tag} indicates the BM tag demodulator admittance. In this section we use the NEC of Fig. 3 circuit to simplify equations and better illustrate each part of the circuit. Fig. 4 describes the NEC in parallel configuration. In Fig. 4, the load Y_{tag} has complex value, where its real part is the conductance G_{tag}, and the imaginary part is the susceptance B_{tag}. The antenna admittance is given by Y_{ant} that has real and imaginary parts equal to G_{ant} and B_{ant}, respectively. Without loss of generality, we set

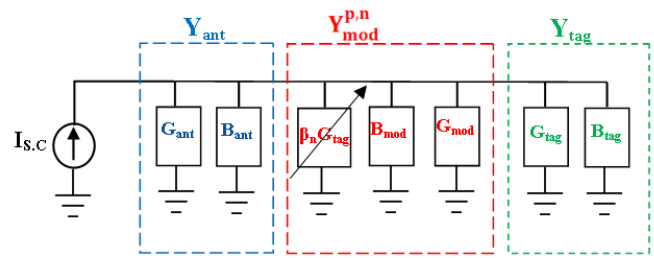

Fig. 4: NEC for the proposed parallel BM tag configuration.

$Y^{p,n}_{mod} = \beta_n G_{tag} + jB_{mod} + G_{mod}$ with $\beta_n \in \mathbb{C}$. B_{mod} and G_{mod} are chosen so the following equations hold

$$B_{ant} + B_{mod} + B_{tag} = 0, \quad \text{and} \quad G_{mod} + G_{ant} = G_{tag}. \quad (2)$$

Thus the modulation load has extra passive parts B_{mod} and G_{mod} which are added in parallel to $\beta_n G_{tag}$ to cancel out the imaginary parts of the antenna and tag and match the real part of the antenna admittance to the real part of tag admittance. We add the matching parts and include them in our model to maximize the received signal in a non-backscattering mode. Using Eq. (2), the equivalent circuit of Fig. 4 is simplified as shown in Fig. 5. Note that $1 \leqslant n \leqslant M$, where M is the

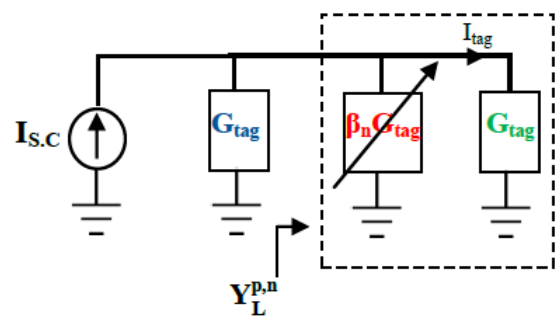

Fig. 5: Simplified NEC of the proposed parallel BM tag configuration.

total number of the backscattered symbols. BM is realized via switching among different values of β_n. The admittance for the load connected to the antenna is

$$Y^{p,n}_L = \beta_n G_{tag} + G_{tag}. \quad (3)$$

The conjugate matched reflection coefficient seen at the antenna port is

$$\Gamma^{p,n}_L = -\frac{\beta_n}{\beta_n + 2}. \quad (4)$$

B. Received and backscattered power

The received power at the BM tag demodulator is calculated using the NEC of the parallel configuration as

$$P^{p,n}_r = \frac{1}{2G_{tag}}|I^{p,n}_{tag}|^2, \quad (5)$$

where $I_{tag}^{p,n} = \frac{I_{S.C}}{2+\beta_n}$ is the current at the demodulator. Thus, the demodulator received power corresponding to each β_n is derived as

$$P_r^{p,n} = \frac{1}{2}\frac{|I_{S.C}|^2}{|2+\beta_n|^2}\frac{1}{G_{tag}}. \tag{6}$$

The backscattered power can be derived from the backscattered electric field as follows

$$P_{scat}^{p,n} = \frac{1}{2z}|E_{scat}^{p,n}|^2, \tag{7}$$

where z is the is the characteristic impedance of the transmission medium. In free space $z = 377$ Ohm. $E_{scat}^{p,n}$ is the BM tag backscattered electric field associated with each modulator load and is calculated using the AST expression of Eq. (1), as

$$E_{scat}^{p,n}(r,\theta,\phi|Z_L^{p,n}) = I(Z_{ant}^*)\underline{E}_r(r,\theta,\phi)(A_{st} - \Gamma_L^{p,n}), \tag{8}$$

where $A_{st} = E_{scat}(r,\theta,\phi|Z_{ant}^*)/(I(Z_{ant}^*)\underline{E}_r(r,\theta,\phi))$ is the antenna structural mode and $\Gamma_L^{p,n}$ is given by Eq. (4) for the parallel configuration. Note that A_{st} has a complex value, which depends on the material and geometry of the antenna, a method to compute the value of A_{st} has been proposed in [29]. Substituting Eq. (4) in Eq. (8) and setting $E_0 = I(Z_{ant}^*)E_r(r,\theta,\phi)$, we have

$$E_{scat}^{p,n}(r,\theta,\phi|Z_L^{p,n}) = E_0\left(A_{st} + \frac{\beta_n}{\beta_n+2}\right). \tag{9}$$

The backscattered electric field can represent the backscattered constellation symbols in BM communication. E_0 has a fixed value for each antenna and does not change with different loads. Thus, we define the backscattered constellation symbols as follows

$$S_n^p = \frac{E_{scat}^{p,n}(r,\theta,\phi|Z_L^{p,n})}{E_0} = A_{st} + \frac{\beta_n}{\beta_n+2}. \tag{10}$$

A_{st} has a fixed value for all backscattered symbols, while the second term changes with the modulator loads and takes different values for each backscattered symbol.

C. Optimization of loads – geometric representation

1) Tag demodulator received power constraint: In BM communication systems, the loads connected to the antenna ($Z_L^{p,n}$) are not conjugate-matched to the antenna impedance and a portion of the received power is reflected toward the reader. This results in downlink data loss compared to a conventional receiver, where the load is conjugate-matched to the antenna. However, by using active loads in BM tag configurations, we can amplify the received power and compensate for the downlink power loss. Thus, we set the following requirement to the received power at the BM tag demodulator

$$P_r^{p,n} \geq P_{match} = \frac{1}{8}\frac{|I_{S.C}|^2}{G_{tag}}, \qquad \forall n \in \{1,..,M\}, \tag{11}$$

where P_{match} is the power delivered to the BM tag demodulator when there is no BM and the demodulator is conjugate-matched to the antenna (conventional receiver circuits). Thus, the demodulator received power constraint is derived in terms of the modulator loads as

$$\frac{1}{2|2+\beta_n|^2} \geq \frac{1}{8}, \qquad \forall n \in \{1,..,M\}. \tag{12}$$

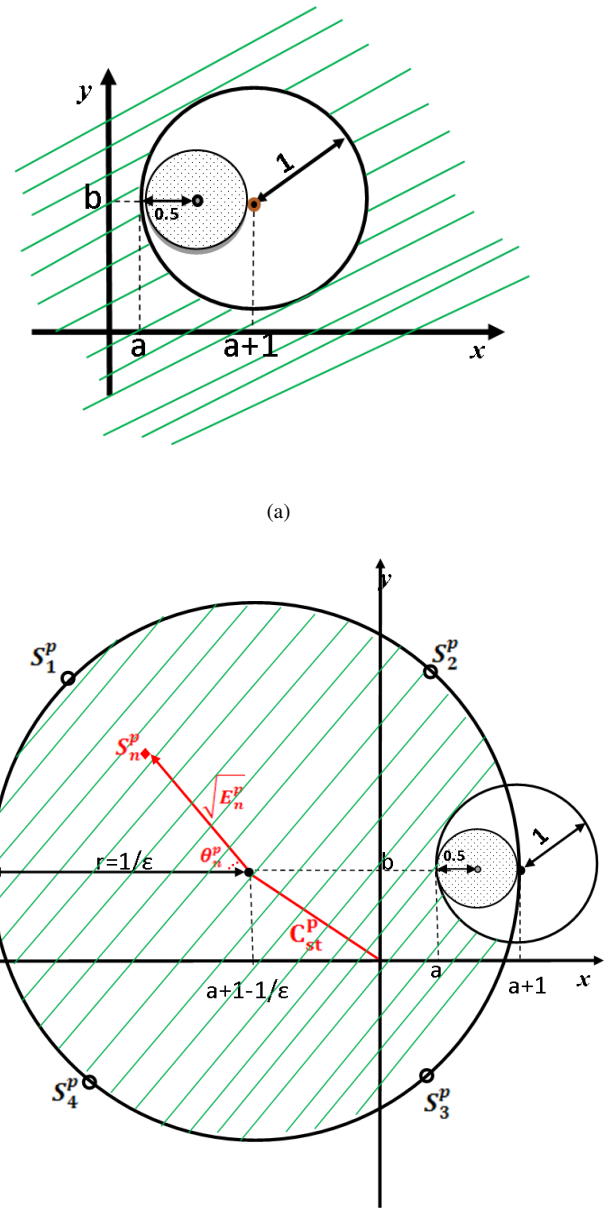

Fig. 6: Backscattered symbols constellation plane corresponding (a) Eq. 12 (hatched area) and $\mathrm{Re}(\beta_n) \geq 0$ (dotted area), and (b) Eq. (12) and $-2+\varepsilon \leq \mathrm{Re}(\beta_n)$ (hatched area).

Since each value of β_n maps to its corresponding backscattered symbol (see Eq. (10)), Eq. (12) can be rewritten as follows

$$\left|\frac{S_n^p - A_{st}}{1 - S_n^p + A_{st}} + 1\right| \leq 1, \qquad \forall n \in \{1,..,M\}. \tag{13}$$

Note that backscattered symbols have real (x_n^p) and imaginary (y_n^p) values in the In-phase/Quadrature (IQ) constellation plane, $S_n^p = x_n^p + jy_n^p$, and the antenna structural mode also has a complex value, $A_{st} = a + jb$. Thus, Eq. (13) can be mapped to the IQ constellation plane as follows

$$(x_n^p - (a+1))^2 + (y_n^p - b)^2 \geq 1. \tag{14}$$

Eq. (14) represents the area outside the unit circle centered at $(a+1, b)$, shown by the hatched area in Fig. 6(a). For passive loads, $\text{Re}(\beta_n) \geq 0$, which maps to the interior of the circle defined by $(x_n^p - (a+0.5))^2 + (y_n^p - b)^2 \leq 0.25$, as illustrated by the dotted pattern in Fig. 6(a).

2) Tag free-oscillation constraint: Any active circuit has the potential to become unstable and start to oscillate. This potential increases as the gain increases [30]. Based on Eq. (9), as β_n moves toward -2, the backscattered gain and the risk of having oscillation increase. Thus, in order to stabilize the circuit and guarantee no oscillations, a tighter bound on $\text{Re}(\beta_n)$ should be applied by setting a new offset, $\varepsilon > 0$, as

$$\text{Re}(\beta_n) \geq -2 + \varepsilon, \qquad \forall n \in \{1, .., M\}. \tag{15}$$

Eq. (15) is mapped to the area inside the circle centered at $C_{st}^p = (a+1-\frac{1}{\varepsilon}, b)$ with radius $\frac{1}{\varepsilon}$, in the constellation plane, as

$$(x_n^p - (a+1-\frac{1}{\varepsilon}))^2 + (y_n^p - b)^2 \leq (\frac{1}{\varepsilon})^2. \tag{16}$$

For $\text{Re}(\beta_n) < -2$, the net resistance of circuit is negative, causing an unstable oscillation.

3) Optimization through geometric representation: The new bound for β_n is the union of the tag demodulator received power constraint (Eq. (14)) and the tag free-oscillation constraint (Eq. (16)) areas, as shown by the hatched area in Fig. 6(b). This area is inside the circle centered at $(a+1-\frac{1}{\varepsilon}, b)$ with radius $\frac{1}{\varepsilon}$ and excluding the area limited by the circle centered at $(a+1, b)$ with radius 1. Each backscattered symbol S_n^p, being represented as

$$S_n^p = C_{st}^p + \sqrt{E_n^p} e^{j(\theta_n^p + \psi^p)}, \qquad \forall n \in \{1, .., M\}, \tag{17}$$

can be placed on the circle with center at $C_{st}^p = (a+1-\frac{1}{\varepsilon}, b)$ and radius $\sqrt{E_n^p}$. Note that C_{st} is the DC term due to backscattering from the antenna (antenna structural scattering). We take into account the antenna structural scattering term when evaluating the average backscattered energy. However, for an average BEP derivation, only the distance between backscatter constellation points matters and this term should be omitted. θ_n^p is the phase of each symbol and ψ^p is the rotation of all symbols. By choosing the backscattered symbols on the circumference of the hatched circle, E_n^p is maximized and both the demodulator received power and oscillation-free constraints are guaranteed.

D. 4-QAM example

In this section, a 4-QAM BM constellation scheme is implemented as an example. We set the constellation symbols in the feasible area of Fig. 6(b) and calculate the value of modulator loads corresponding to each symbols. The 4-QAM constellation symbols are S_1^p, S_2^p, S_3^p, and S_4^p, shown in Fig. 6(b). These symbols are chosen for maximum distance among the backscattered symbols. For each of these symbols, the corresponding modulator load admittance is calculated and given by $Y_{mod}^{p,n}$ in Table I where $\varepsilon = 0.06$, $\psi^p = 0$, $A_{st} = 1$ and $B_{mod} = G_{mod} = 0$ (the antenna and demodulator are conjugate-matched). Otherwise, B_{mod} and G_{mod} should be added to $Y_{mod}^{p,n}$. We also report the corresponding values of β_n for $G_{tag} = 1/50$ Ohm.

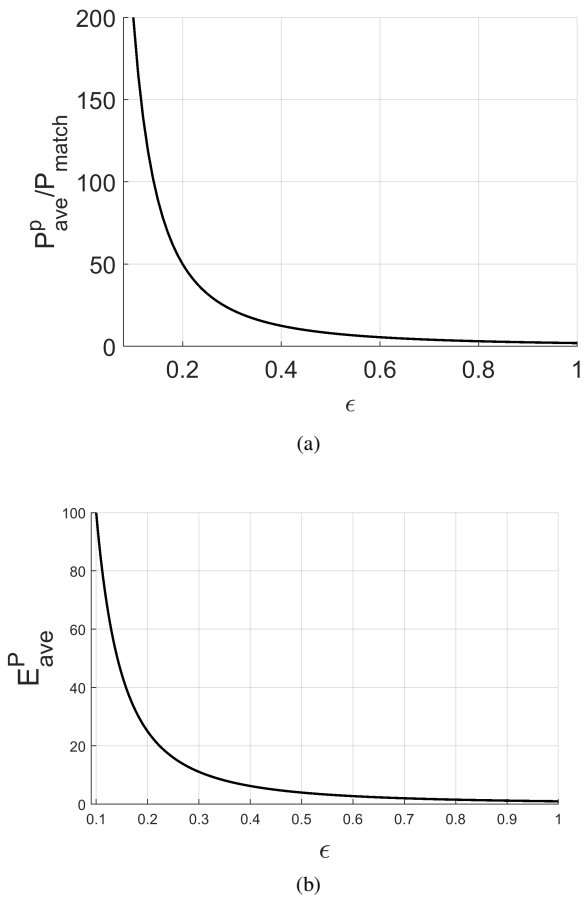

Fig. 7: (a) Average received power at the BM tag demodulator, and (b) average power of backscattered symbols.

The average received power at the BM tag demodulator is calculated as

$$P_{ave}^p = \frac{1}{4}\sum_{n=1}^{4} P_r^{p,n} = \frac{1}{4}\sum_{n=1}^{4} \frac{4}{|2+\beta_n|^2} P_{match}, \; \forall n \in \{1, .., 4\}, \tag{18}$$

which is plotted as a function of ϵ, as shown in Fig. 7(a). As ϵ gets smaller values (moves toward the oscillation point), the average power delivered to the tag demodulator increases. The average power of backscattered symbols is calculated as

$$E_{ave}^p = \frac{1}{4}\sum_{n=1}^{4} E_n^p = (\frac{1}{\varepsilon})^2, \qquad \forall n \in \{1, .., 4\}, \tag{19}$$

E_{ave}^p as a function of ϵ is plotted in Fig. 7(b). As ϵ gets smaller, the average backscattered symbols power increases. The average received power at the BM tag demodulator and the backscattered symbols power show the same behavior. Thus, as we move toward oscillation point, both demodulator received power and backscattered symbols power increase.

IV. BM Tag Series Configuration

In this section, we introduce series tag configuration. Like the previous section, we first present the proposed BM tag

TABLE I: 4-QAM constellation symbols example and their corresponding β_n and modulator loads. $Y_{mod}^{p,n}$

S_1^p	-26.4+11.7j	β_1	-1.94+0.024j	$Y_{mod}^{p,1}$	-0.038+0.0005j
S_2^p	-2.88+11.7j	β_2	-1.94+0.144j	$Y_{mod}^{p,2}$	-0.038+0.0029j
S_3^p	-2.88-11.7j	β_3	-1.94-0.144j	$Y_{mod}^{p,3}$	-0.038-0.0029j
S_4^p	-26.4-11.7j	β_4	-1.94-0.024j	$Y_{mod}^{p,4}$	-0.038-0.0005j

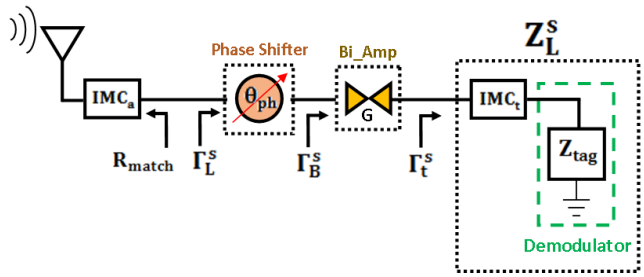

Fig. 8: Proposed series BM tag configuration schematic.

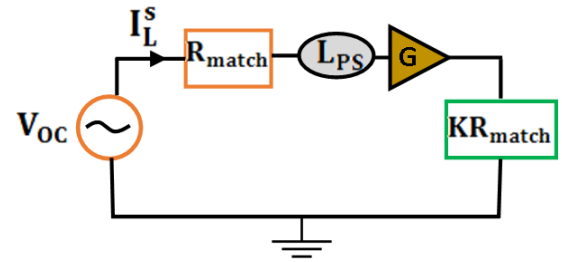

Fig. 9: TEC of the proposed series BM tag configuration.

structure and derive the received and backscattered power. Based on the geometric representation of the backscattered symbols, we optimize the BM tag modulator loads to implement the desired BM constellation map, maximize the backscattered power and guarantee at least P_{match} at the demodulator.

A. Series configuration schematic

The proposed series BM tag configuration includes six parts: *i*) the antenna, *ii*) the antenna impedance matching circuit (IMC_a), *iii*) the digital phase shifter, *iv*) the bidirectional amplifier (Bi-Amp), *v*) the impedance matching circuit of the tag demodulator (IMC_t), and *vi*) the BM tag demodulator (Z_{tag}), as shown in Fig. 8. Bidirectional amplifiers are two-port amplifiers, which can amplify the incoming signal along both directions. Digital phase shifters are used to change the phase of electromagnetic waves, controlled by digital bits. The digital phase shifter, bidirectional amplifier, and tag demodulator have standard input impedance equals to R_{match} (usually 50 Ohm), and the antenna is matched with them using the IMC_a. To implement a BM link, we make a deliberate mismatch (Γ_t^s) using the IMC_t at the tag demodulator interface. Γ_t^s is the reflection coefficient seen at the BM tag demodulator interface. The IMC_t is a passive lossless impedance matching circuit which transfers Z_{tag} to KR_{match}, where K is a positive real number. The value of K and bidirectional amplifier gain G, determine the amplitude of the backscattered symbols. In order to modulate the amplitude of backscattered signal, we vary K, using an RF switch at the IMC_t port. The symbol phases are set using the phase shifter. Therefore, to implement a PSK constellation, K and G are fixed. To generate a QAM constellation, we can change the amplitude of the backscattered symbols by varying the values of K via switching among different IMC_t structures.

B. Received and backscattered power

To make the equation more trackable, we fixed the values of G and K and switched among different values of the phase shifter (M-PSK constellation). The received power at the BM tag demodulator, denoted by P_r^s, has the same value for all different values of the phase shifter and is derived using the TEC of the proposed series configuration, shown in Fig. 9. We assume to have a phase shifter with average insertion loss L_{ps}, and lossless impedance matching circuits. We also assume that the bidirectional amplifier has the same forward and backward power gain G. Based on the TEC shown in Fig. 9, the received power at KR_{match} is

$$P_r^s = \frac{1}{2} K R_{match} |I_L^s|^2 \quad \text{where} \tag{20}$$
$$I_L^s = \sqrt{G L_{ps}} \frac{V_{OC}}{R_{match} + K R_{match}}.$$

Thus,

$$P_r^s = \frac{1}{2}\left(\frac{V_{OC}}{K+1}\right)^2 \frac{G L_{ps} K}{R_{match}} = P_{match} G L_{ps} \frac{4K}{(K+1)^2}. \tag{21}$$

We use the AST to derive the backscattered power at the series BM tag interface

$$P_{scat}^{s,n} = \frac{1}{2z} |E_{scat}^{s,n}|^2 \text{ with } E_{scat}^{s,n}(r,\theta,\phi|Z_L^{s,n}) = E_0(A_{st} - \Gamma_L^{s,n}). \tag{22}$$

We set the backscattered symbols to the normalized backscattered electric field, $S_n^s = (A_{st} - \Gamma_L^{s,n})$, where $\Gamma_L^{s,n}$ is the power reflection coefficient seen at the input port of the phase shifter. To derive the expression of $\Gamma_L^{s,n}$, we first need to find the reflection coefficient Γ_B^s, seen at the bidirectional amplifier interface. Γ_B^s depends on the structure of the bidirectional amplifier. Using the bidirectional amplifier circuit proposed in [22], Γ_B^s can be expressed as

$$\Gamma_B^s = -G\Gamma_t^s = -G\left(\frac{K-1}{K+1}\right). \tag{23}$$

Therefore, $\Gamma_L^{s,n}$ is given by

$$\Gamma_L^{s,n} = \Gamma_B^s e^{-j2\theta_{ph}^n} L_{ps} = -G L_{ps}\left(\frac{K-1}{K+1}\right) e^{-j2\theta_{ph}^n}, \tag{24}$$

where θ^n_{ph} is the phase of the phase shifter for backscattered symbol S^s_n. Since the backscattered waves pass the phase shifter twice, we set the phase shifter delay as

$$\theta^n_{ph} = -\frac{\theta^s_n}{2} = -\frac{2n-1}{2M}\pi, \qquad \forall n \in \{1,..,M\}, \tag{25}$$

where M is the constellation size, θ^s_n is the phase of each backscattered symbol S^s_n and ψ^s represents the rotation of all symbols. Thus, the backscattered symbols, S^s_n, can be defined by

$$S^s_n = A_{st} + GL_{ps}\frac{K-1}{K+1}e^{j(\theta^s_n+\psi^s)}, \quad \forall n \in \{1,..,M\}, \tag{26}$$

C. Optimization of loads – the geometric representation

1) Tag demodulator received power constraint: For the proposed series BM tag configuration, we set the same power requirement at the tag demodulator as for the parallel configuration,

$$P^s_r \geq P_{match}. \tag{27}$$

We derive upper and lower bound of K, using Eq. (27) and Eq. (21), as

$$\overbrace{(\sqrt{GL_{ps}} - \sqrt{GL_{ps}-1})^2}^{K_L} \leq K \leq \overbrace{(\sqrt{GL_{ps}} + \sqrt{GL_{ps}-1})^2}^{K_U}. \tag{28}$$

Eq. (28) shows that to guarantee the tag demodulator power constraint, for a given value of G, $K \in [K_L, K_U]$. Also increasing the gain of the bidirectional amplifier or decreasing the loss of the phase shifter increase the range of K. Note that K determines the value of P^s_r, see Eq. (21). For example, if $K = 1$ then $P^s_r = GL_{ps}P_{match}$, and if $K = K_L$ or $K = K_U$ then $P^s_r = P_{match}$.

2) Tag oscillation-free constraint: For the series configuration, the oscillation-free constraint is related to the gain of the bidirectional amplifier. There are several types of bidirectional amplifiers proposed in literature [22], [31]–[33]. In this section we are not concerned about the oscillation criteria in the circuit, since G is reported for the oscillation-free condition.

3) Optimization through geometric representation: Each value of K maps to its corresponding backscattered symbol, see Eq. (26). Thus we can rewrite Eq. (28) in terms of S^s_n, to derive the geometric representation of feasible backscattered constellation area,

$$|S^s_n - A_{st}| \leq \sqrt{{GL_{ps}}^2 - GL_{ps}}, \qquad \forall n \in \{1,..,M\}. \tag{29}$$

For the complex constellation symbols in IQ plane, $S^s_n = x^s_n + jy^s_n$ and $A_{st} = a + jb$, Eq. (29) maps to the circle centered at (a, b) with radius $\sqrt{{GL_{ps}}^2 - GL_{ps}}$, shown by the hatched area in Fig. 10,

$$(x^s_n - a)^2 + (y^s_n - b)^2 \leq {GL_{ps}}^2 - GL_{ps}. \tag{30}$$

Note that each backscattered symbol S^s_n is represented as

$$S^s_n = C^s_{st} + \sqrt{E^s_n}e^{j(\theta^s_n+\psi^s)}, \qquad \forall n \in \{1,..,M\}, \tag{31}$$

and can be placed on a circle with center $C_{st} = (a, b)$ and radius $\sqrt{E^s_n} = GL_{ps}\left|\frac{K-1}{K+1}\right|$.

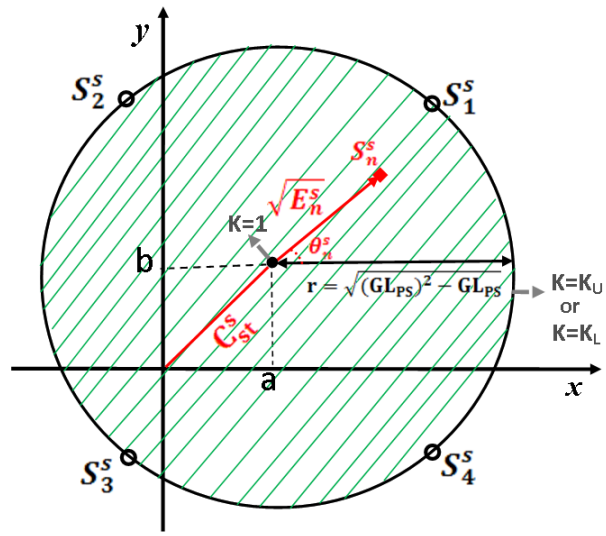

Fig. 10: Backscatter symbols constellation plane corresponding to $K_L \leq K \leq K_U$.

D. 4-QAM example

In this section a 4-QAM BM constellation scheme is implemented, as an example. We use the geometric representation of Fig. 10 to choose the backscattered symbols S^s_n. The 4-QAM constellation symbols S^s_1, S^s_2, S^s_3 and S^s_4 are picked, as shown in Fig. 10. These symbols are chosen on the circumference of the hatched circle to maximize the distance among the backscattered symbols. As shown in Fig. 10, on the circumference of the hatched circle $K = K_U$ and $E^s_n = {GL_{ps}}^2 - GL_{ps}$. For G = 13 dB, $A_{st} = 1$, $\psi^s = 0$ and L_{ps} = 3 dB, backscattered symbols and their corresponding phase shifter values are given in Table II. The average received power at

TABLE II: 4-QAM constellation symbols example and their corresponding phase shifter values.

S^s_1	7.7+6.7j	θ^1_{ph}	$-22.5°$
S^s_2	-5.7+6.7j	θ^2_{ph}	$-67.5°$
S^s_3	-5.7-6.7j	θ^3_{ph}	$-112.5°$
S^s_4	7.7-6.7j	θ^4_{ph}	$-157.5°$

the BM tag demodulator for 4-QAM constellation is

$$P^s_{ave} = \frac{1}{4}\sum_{n=1}^{4} P^{s,n}_r = P_{match}GL_{ps}\frac{4K}{(K+1)^2}, \forall n \in \{1,..,4\}, \tag{32}$$

For a fixed value of G and L_{ps}, we plotted P^s_{ave} as a function of K in Fig. 11(a). At $K = 1$, $P^s_{ave} = GL_{ps}P_{match}$ and at $K = K_L$ or $K = K_U$, $P^s_{ave} = P_{match}$. If $K \notin [K_L, K_U]$, then $P^s_{ave} < P_{match}$. The average power of the backscattered symbols for 4-QAM constellation is calculated as

$$E^s_{ave} = \frac{1}{4}\sum_{n=1}^{4} E^s_n = \left(GL_{ps}\frac{K-1}{K+1}\right)^2, \qquad \forall n \in \{1,..,4\}, \tag{33}$$

E^s_{ave} is plotted in Fig. 11(b) as a function of K for a fixed value of G. At $K = 1$, $E^s_{ave} = 0$, and at $K = K_L$ or

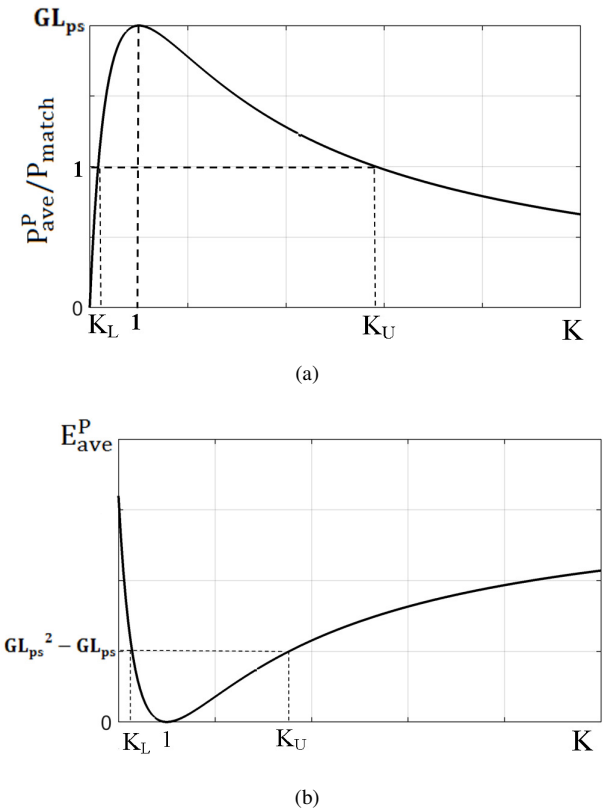

Fig. 11: (a) Average received power at the tag demodulator, and (b) the average backscattered symbols power.

$K = K_U$, $E^s_{ave} = (GL_{ps})^2 - GL_{ps}$. Fig. 11 shows that there is a tradeoff between the received power at the tag demodulator P^s_{ave} and backscattered symbols power E^s_{ave}. As the value of K moves closer to K_L or K_U, E^s_{ave} increases but P^s_{ave} decreases. This is contrary to the parallel configuration, where when ϵ moves toward 0, both E^p_{ave} and P^p_{ave} increase.

V. Average Bit Error Probability

Since we guaranteed at least P_{match} at the tag demodulators, the average bit error probability (BEP) at the reader will be used to compare the two proposed active BM tag configurations: Series and parallel. Due to the particularity of the channel between the BM tag and the reader, the distribution of the signal-to-noise ratio (SNR) should be studied before handling the conditional BEP and then the average BEP.

A. SNR distribution

We define P^p_d and P^s_d as the received power at the reader for the parallel and series BM tag configurations, respectively. We derived their expressions using the AST for a fading channel as

$$P^{p,s}_d = P_t G^{TX}_d L_{rt} |u_t.u_{inc}|^2 G^2_t L_{tr} |u_r.u_{scat}|^2 G^{RX}_d |h_{rt} h_{tr}|^2 \times |A_{st} - \Gamma^{p,s}_L|^2 + N_t F_t |\Gamma^{p,s}_L|^2 L_{tr} |h_{tr}|^2 + N_r F_r, \quad (34)$$

where P_t is the transmitted power from the reader to the tag, G^{TX}_d and G^{RX}_d are the reader's transmitter (TX) and receiver (RX) antenna gains, L_{rt} and L_{tr} are path-loss associated with signal from reader-to-tag and tag-to-reader, and $|\hat{u}_t.\hat{u}_{inc}|$ and $|\hat{u}_r.\hat{u}_{scat}|$ account for the possible polarization mismatch between (incident waves and tag antenna) and (backscattered waves and reader antenna), respectively. h_{rt} and h_{tr} are the normalized reader-to-tag and tag-to-reader channel gains. N_t and F_t are thermal noise power and noise figure at the tag, amplified by tag backscattered gain and received at the reader through channel h_{tr} with path loss L_{tr}. N_r and F_r are thermal noise power and noise figure at the reader. It has been shown in [34], that the equivalent noise at reader due to the tag thermal noise is much less significant than the reader's own thermal noise. Thus, the instantaneous SNR at reader, $\gamma^{p,s}$, that is given by

$$\gamma^{p,s} = \gamma_0 |h_{rt} h_{tr}|^2 |A_{st} - \Gamma^{p,s}_L|^2, \quad (35)$$

where γ_0 is the average SNR received at the reader, normalized by the backscattered symbol power, given by

$$\gamma_0 = \frac{P_t G^{TX}_d}{N_r F_r} L_{rt} |u_t.u_{inc}|^2 G^2_t L_{tr} |u_r.u_{scat}|^2 G^{RX}_d. \quad (36)$$

The backscatter symbol, $S^{p,s} = A_{st} - \Gamma^{p,s}_L$, is given by Eq. (17) and (31) for parallel and series BM tag configurations, respectively. The offsets C^p_{st} and C^s_{st} do not contribute on the BEP derivation. The contributed SNR in BEP, $\gamma^{p,s}_{eff}$, for the parallel and series configurations is

$$\gamma^{p,s}_{eff} = \gamma_0 |h_{rt} h_{tr}|^2 E^{p,s}_{ave}. \quad (37)$$

The measurements in [35] showed that the backscattered signal has deeper fades than the signal from a one-way link because the fading on the backscattered signal is the product of the downlink fading and the uplink fading. Thereby, the best model to fit the backscattered signal fading is the product Rician distribution. It is worth mentioning that some measurements of the product Rician distribution parameters were described in [35]. Furthermore, it was proven in [36] that the Rician distribution is valid for line of sight (LOS) models, and that the product-Rician with independent segments is valid for local area, the measurements therein affirm that the backscatter channel can be approximated by a product-Rician distribution with independent segments for monostatic and bistatic scenarios, where the reader transmitter and receiver antennas are separated and adequately spaced. In addition, in [37], the channel segments in RFID system were assumed independent, based on CDF measurements. Hence, the channel coefficients, $|h_{rt}|$ and $|h_{tr}|$, are modeled by Rician distribution with probability density function (PDF) given in [38, Eq. (2.15)] and distribution factors k_{rt} and k_{tr} for downlink and uplink, respectively. The PDF of the product of two independent Rician random variables, $|h_{rt} h_{tr}|^2$, can be obtained in integral form. However, an infinite sum representation was derived in [39], where low number of terms can be considered with small truncation errors, depending on the Rician factors (e.g. for $k_{tr} = k_{rt} = 3$ dB, the truncation error reduces to 10^{-15} with 600 terms). For that reason and by considering a

change of variable, the PDF of the SNR can be derived using [39, Eq. (24)] as

$$f^{p,s}_{\gamma_{eff}}(\gamma) = \frac{2\kappa e^{-k_{tr}-k_{rt}}}{\gamma_0 E^{p,s}_{ave}} \sum_{g,l=0}^{\infty} \frac{k^g_{tr} k^l_{rt}}{(g!l!)^2} \left(\frac{\kappa\gamma}{\gamma_0 E^{p,s}_{ave}}\right)^{\frac{g+l}{2}} \times K_{g-l}\left(\sqrt{\frac{4\kappa\gamma}{\gamma_0 E^{p,s}_{ave}}}\right), \quad (38)$$

where $\kappa = (1+k_{tr})(1+k_{rt})$ and $K_g(\cdot)$ is the g-th order modified Bessel function of the second kind [40, Eq. (9.6.24)].

B. Average BEP

Through an additive white Gaussian noise (AWGN) channel, the conditional BEP of 4-QAM constellation map is given in [38, Eq. (8.16)] by

$$\eta^{p,s}_e = Q\left(\sqrt{\gamma^{p,s}_{eff}}\right), \quad (39)$$

where $Q(\cdot)$ is the Gaussian Q function [38, Eq. (4.1)]. The average BEP is obtained by averaging the conditional BEP over the distribution of the SNR

$$\overline{\eta}^{p,s}_e = \int_0^{\infty} \eta^{p,s}_e \; f_{\gamma^{p,s}_{eff}}(\gamma) d\gamma. \quad (40)$$

Thus, by substituting Eq. (38) and Eq. (39) in Eq. (40), we get the average BEP as follows

$$\overline{\eta}^{p,s}_e = \frac{2\kappa e^{-k_{tr}-k_{rt}}}{\gamma_0 E^{p,s}_{ave}} \sum_{g,l=0}^{\infty} \frac{k^g_{tr} k^l_{rt}}{(g!l!)^2} \int_0^{\infty} \left(\frac{\kappa\gamma}{\gamma_0 E^{p,s}_{ave}}\right)^{\frac{g+l}{2}} \times Q(\sqrt{\gamma}) K_{g-l}\left(\sqrt{\frac{4\kappa\gamma}{\gamma_0 E^{p,s}_{ave}}}\right) d\gamma. \quad (41)$$

To find a compact expression for Eq. (41), an integral of the form $\int_0^{\infty} x^{g+l+1} Q(x) K_{g-l}(ax) dx$ should be evaluated for some positive number a. Using alternative expressions of the Q function and the Bessel function in terms of the Meijer's G function (MGF) [41, Eq. (2.9.1)], available in [42, Eq. (8.4.14.2)] and [41, Eq. (2.9.19)], respectively, the integral becomes an integral of the product of two MGFs, which can be solved using the integral identity [41, Eq. (2.8.4)]. Therefore, the average BEP of 4-QAM BM scheme can be expressed as

$$\overline{\eta}^{p,s}_e = \frac{e^{-k_{tr}-k_{rt}}}{2\sqrt{\pi}} \sum_{g,l=0}^{\infty} \frac{k^g_{tr} k^l_{rt}}{(g!l!)^2} \, \mathrm{G}^{2,2}_{2,3}\left[\frac{2\kappa}{\gamma_0 E^{p,s}_{ave}} \middle| \begin{matrix} 1, \frac{1}{2} \\ 1+g, 1+l, 0 \end{matrix}\right]. \quad (42)$$

VI. Simulation Results

This section shows some selected numerical results supported by Monte Carlo MATLAB® simulations to illustrate the average BEP at the reader. To compare the proposed tag configurations, we used γ_0 as the reference SNR and plotted the average BEP derived in Eq. (42), versus γ_0. We assume 4-QAM constellation scheme and the maximum backscattered power as an example. To conclude the paper, we also compare the average BEP normalized to DC power consumption to evaluate the performance of parallel/series configurations, passive tags, active point to point tags and ZigBee modules.

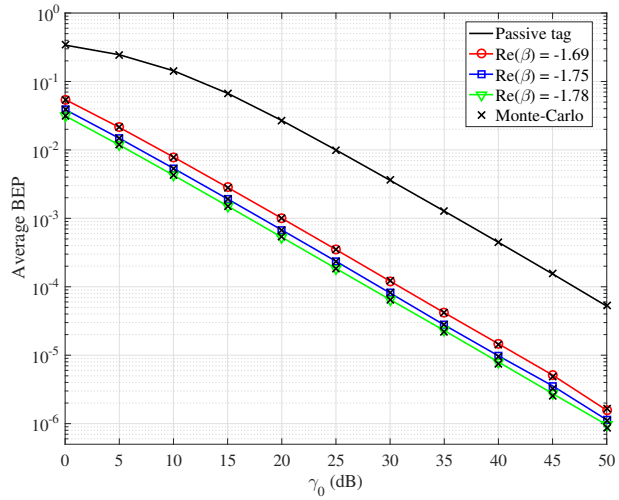

Fig. 12: Average BEP at the reader for the parallel BM tag configuration. The lines denote the analytical results while the cross markers denote the Monte-Carlo simulations.

A. Parallel BM tag configuration

For the parallel configuration, we run the simulations and plot the average BEP at the reader, for different values of Re(β) and maximum backscattered power, shown in Fig. 12. Note that the value of the average backscattered symbols power E^p_{ave} can be derived from the value of Re(β), based on Eq. (19). We assume Rician fading with Rician factors $k_{rt} = k_{tr} = 2.7$ dB [35]. We set three different values of Re(β): -1.78, -1.75, and -1.69. These numbers are practical values that set the circuit far from the oscillation point, since they correspond to reflection gain of 18.4 dB, 17 dB, and 14 dB, respectively. Based on [43], a tunnel-diode reflection amplifier starts to oscillate for more than 20 dB gain. Thus, for Re(β)>-1.82 ($\epsilon > 0.18$), the circuit stays stable and this choice guarantees no oscillations. We also plotted the average BEP of passive BM tags to better highlight the impact of active loads on the reader average BEP. Like parallel and series BM tags, the maximum backscattered symbols power for a passive tag is the square of its constellation circle radius. The constellation circle of passive tags is shown with the dotted area in Fig. 6(a). Thus, $E^{passive}_{ave} = (0.5)^2$. For example of tunnel-diode based negative resistance the DC power consumption is 0.2 mW [44]. As expected, if we pick Re(β) close to the oscillation point, the backscattered power increases and the average BEP at the reader decreases as a result. For the conventional passive BM tag, the reader needs γ_0 to be at least 47 dB to guarantee an average BEP of 10^{-4}. For the parallel BM tag configuration, we decreased this value to 31 dB, 29 dB and 28 dB for Re(β) $= -1.69$, Re(β) $= -1.75$ and Re(β) $= -1.78$, respectively. Based on the approximate theoretical expression of [8, Eq. (19.20)], for 19 dB SNR gain at the reader, the uplink range increases up to 60 %. It is noticeable that this range gain is achieved at the expense of more complex, larger and battery-dependent circuit compared to a passive tag circuit.

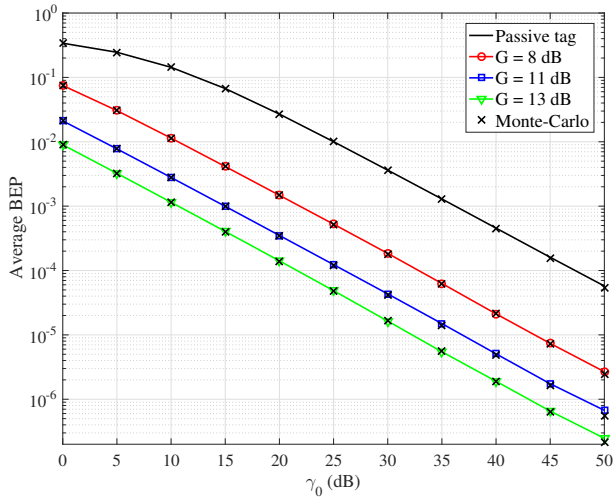

Fig. 13: Average BEP at the reader for the series BM tag configuration. Phase shifter insertion loss=3 dB. The lines denote the analytical results while the cross markers denote the Monte-Carlo simulations.

B. Series BM tag configuration

For the series BM tag configuration, we plot the average BEP for $G = 8$ dB, $G = 11$ dB, and $G = 13$ dB, and phase shifter insertion loss of 3 dB, as shown in Fig. 13. Note that the average backscattered symbols power is derived from the values of GL_{ps} based on Eq. (33). We chose these values of gain based on [19], where oscillation starts after 15 dB gain for a transistor-based bidirectional amplifier. The transistor-based bidirectional amplifier in [19] consumes 2.4 mW DC power and for a 6-bit digital phase shifter from QORVO, with part number QPC2108, this number is 2 mW. We set $K = K_L$ to maximize the backscattered power and assume Rician fading with Rician factors $k_{rt} = k_{tr} = 2.7$ dB. Like the parallel configuration, we also plot the average BEP at the reader for passive BM tags. As expected, by increasing the gain of the bidirectional amplifier the average BEP at the reader decreases. Note that high-gain bidirectional amplifiers (generally all amplifiers) are prone to oscillate. Thus, there is a tradeoff between the gain and stability of the amplifier, which should be taken into account. Compared to a passive tag, for $G = 8$ dB, $G = 11$ dB and $G = 13$ dB, a maximum SNR gain of 15 dB, 22 dB and 25 dB could be theoretically achieved at the reader for an average BEP of 10^{-4}. The SNR gains achieved in series BM tag configuration are larger than the SNR gains in parallel BM tag configuration. The reason lies in the BM tag configurations design. In the series tag configuration, we can set the receive power at tag demodulator to the least acceptable value P_{match}, and backscatter the rest of power toward the reader. Also the backscattered signal is amplified two times by the bidirectional amplifier, which further increases the backscattered power. Contrary to the series tag configuration, in the parallel tag configuration the received power at tag demodulator and the backscattered power increase together.

C. Parallel and series tag comparison

To compare the proposed parallel and series BM tag configurations, several factors should be weighted, which include but are not limited to the circuit complexity, the power consumption, the size, the BEP at the reader, the received power at the tag demodulator and the feasibility of implementing the desired BM constellation map. These factors must be ranked by importance for individual applications. The comparison through all the mentioned factors between the two proposed configurations is beyond the scope of this paper. In this paper, we just compare the parallel and series BM tag configurations based on the average BEP at the reader. In the series tag configuration, we consider the transistor-based bidirectional amplifier structure proposed in [19], which oscillates for $G > 15$ dB. To sit far from oscillation point, we consider G=10 dB (5 dB less gain). In the parallel tag configuration, we used a tunnel diode-based negative resistance parallel with the the tag demodulator as a one-port reflection amplifier. Based on [43], it starts to oscillate when its reflection gain is more than 20 dB. Again, to be on the safe side and away from oscillation, we picked 15 dB gain (5 dB less than oscillation border) of reflection amplifier which corresponds to $\text{Re}(\beta_n) = -1.7$. Here, we also add the plot for bidirectional amplifier gain of 15 dB, to compare the series and parallel configurations, when both have the same reflection gain. The results are

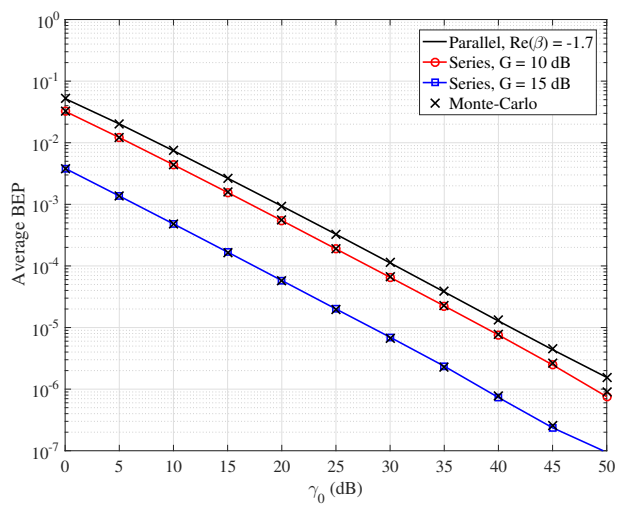

Fig. 14: Comparison between parallel and series tag average BEP at the reader. Phase shifter insertion loss=3 dB. The lines denote the analytical results while the cross markers denote the Monte-Carlo simulations.

shown in Fig. 14. For the same oscillation-free constraint (5 dB less than oscillation border gain), the series configuration shows better performance in case of average BEP at the reader. For the same gain condition (G=15 dB and Re(β)=-1.7), the series configuration has maximum SNR gain of 12 dB is compared with parallel configuration at average BEP of 10^{-4}. The bidirectional amplifier and digital phase shifter used in the series configuration are complex circuits with higher power consumption compared with the parallel configuration

elements, which is the price of better BEP performance at the reader.

D. Average BEP normalized to DC power consumption

In this section, we normalize the average BEP at reader to the DC power consumption of i) passive RFID tag, ii) parallel configuration, iii) series configuration, iv) active point to point RFID tag, and v) ZigBee module. To do so, we use the following assumptions:

1) The value of reader's DC power consumption can vary based on application and standard used in its structure. For a gain-adjusted active RFID reader (217002) from GAORFID company, the total DC power consumption is 450 mW.
2) a) In the parallel configuration, for the tunnel diode based negative resistance, the DC power consumption is 0.2 mW. For the micro-controller and RF switch, we refer to AT89S51 ATMEL and RF switch 63DR *Mini-Circuit* as an example where the consumed DC power are 75 mW and 150 μW, respectively. We set Re$(\beta) = -1.78$.
   b) The series configuration consumes 2.4 mW +2 mW= 4.4 mW for bidirectional amplifier and phase shifter. The micro-controller AT89S51 ATMEL and RF switch 63DR *Mini-Circuit* use a DC power of 75 mW and 150 μW, respectively. The bidirectional gain is $G = 13$ dB and phase shifter insertion loss is 3 dB.
3) For active point to point RFID tags, there are also different prototypes with various values of power consumption. We refer to [45], which studied three different prototype of active RFIDs. As an example we consider an active IEEE 802.11 RFID tag which uses 300 mW power.
4) For ZigBee, we refer to Zigbee Module (802.15.4) XBee, from Digi International. Based on its data sheet, the battery power consumption is 396 mW for PRO model.
5) For the BM group, the channel gain is $|h_{rt}h_{tr}|^2$, while for an active point to point RFID tag and ZigBee it is $|h_{tr}|^2$.
6) In active point to point RFID tag and ZigBee, there is a one-way path loss associated with the signal, L_{tr}.

In order to normalize the average BEP at reader to the DC power consumption of each tag, we used a normalization coefficient N_{PC} at the effective SNR derivation (Eq. 37), as follows:

i) For the passive RFID tag, N_{PC}=1.
ii) For the parallel configuration, N_{PC}=(reader DC power consumption)/(reader DC power consumption+ parallel DC power consumption).
iii) For the series configuration, N_{PC}=(reader DC power consumption)/(reader DC power consumption+ series DC power consumption).
iv) For the active P2P RFID tag, N_{PC}=(reader DC power consumption)/(reader DC power consumption+ active DC power consumption).
v) For the ZigBee module, we set $N_{PC} = 0.5$, since ZigBee is a separate wireless node and not associated with a reader.

The simulation results of the re-derived average BEP at reader normalized to DC power consumption are shown in Fig. 15. As one can see, parallel and series configuration perform

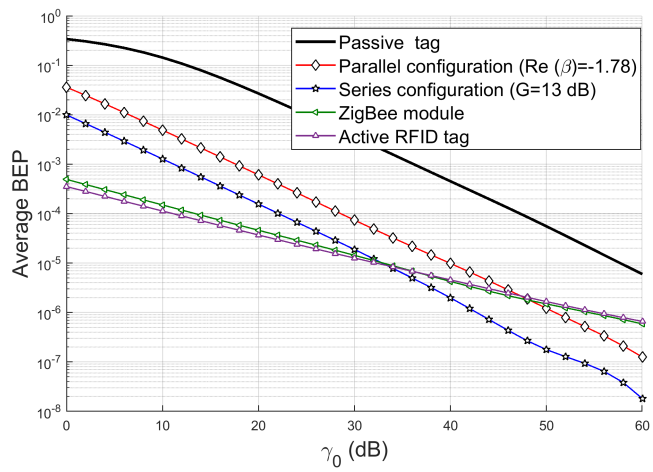

Fig. 15: Average BEP at reader normalized to DC power consumption at each tag structure.

better than passive tag. In the low SNR regime (large distance between reader and tag), active point to point RFID tag and ZigBee outperform passive and parallel/series configurations. This is due to a one-way path loss associated with non BM structures, where the signal falls as the square of the distance $(1/r^2)$, rather than a two-way path loss in BM structures $(1/r^4)$. Note that for non BM structures, the BEP curve slope is half of the BM structures, since the path loss and channel gain in non BM depend on the square root of BM. Thus, the average BEP falls quicker as we increase γ_0 for parallel and series configuration compared to an active tag and a ZigBee module.

In the high SNR regime, on the other hand, the proposed parallel and series configurations start to outperform active point to point RFID and ZigBee. Parallel and series configurations consume less DC power compared to point to point RFID tag and ZigBee. Please note that by increasing G and decreasing Re(β), the backscattered gain is increased and even a better performance in parallel/series configurations can be obtained. It is worth mentioning that better performance of active RFID tag and ZigBee comes with the price of having a separate transmitter in the tag, with large complexity, cost and power consumption.

VII. Conclusion

In this paper, we propose two active two-way BM tag configurations. The first BM tag configuration, called parallel configuration, uses a negative resistance in parallel with the tag demodulator. The second BM tag configuration, called

series configuration, uses a bidirectional amplifier in series with the tag demodulator. Using AST and TEC/NEC, we accurately model and optimized each BM tag configuration to provide at least a power P_{match} at the tag demodulator while exhibiting maximum difference in the backscattered field and implementing the desired constellation map. For both BM tags, we propose a new geometric representation of the backscattered symbols to optimize the tag modulator loads. We derive a closed-form expression of the average BEP at the reader in a Rician fading channel environment and use it to compare parallel and series configurations with a conventional passive BM tag. The simulation results allow us to conclude that, compared to a passive BM tag circuit, the proposed BM tag configurations can implement the desired constellation and considerably increase the communication range.

REFERENCES

[1] H. Stockman, "Communication by means of reflected power," *Proc. of the IRE*, vol. 36, no. 10, pp. 1196–1204, Oct. 1948.

[2] W. ChangCheng, L. DongBo, and H. JiaBin, "Process of reading and writing the tag of the motor vehicle electrical identification system based on the RFID technology," in *Proc. of the Asia-Pacific Signal and Information Processing Association Annual Summit and Conference (APSIPA'2013)*, Kaohsiung, Taiwan, Oct. 2013, pp. 1–5.

[3] S. Qi, Y. Zheng, M. Li, Y. Liu, and J. Qiu, "Scalable industry data access control in rfid-enabled supply chain," *IEEE/ACM Transactions on Networking*, vol. 24, no. 6, pp. 3551–3564, Dec. 2016.

[4] S. P. Arunachalam, M. Sir, G. Marisamy, A. Sadosty, D. Nestler, T. Hellmich, and K. Pasupathy, "Identifying factors influencing patient alone time at the emergency department using RFID data: What is next?" in *Proc. of the IEEE EMBS International Conference on Biomedical Health Informatics (BHI'2017)*, Orlando, FL, USA, Feb. 2017, pp. 225–228.

[5] B. Smida, "Communicating data using backscatter modulation," *Filed US Patent 2013-SMID-66564-01*, 2013.

[6] B. Smida and S. Khaledian, "ReflectFX: In-band full-duplex wireless communication by means of reflected power," *IEEE Transactions on Communications*, vol. 65, no. 5, pp. 2207–2219, May 2017.

[7] S. Khaledian, F. Farzami, B. Smida, and D. Erricolo, "A power-efficient implementation of in-band full-duplex communication system (ReflectFX)," in *Proc. of International Symposium on Signal, Image, Video and Communications (ISIVC)*, Nov 2016, pp. 242–246.

[8] J. Kimionis, A. Georgiadis, A. Collado, and M. M. Tentzeris, "Enhancement of RF tag backscatter efficiency with low-power reflection amplifiers," *IEEE Transactions on Microwave Theory and Techniques*, vol. 62, no. 12, pp. 3562–3571, Dec. 2014.

[9] F. Amato, C. W. Peterson, B. P. Degnan, and G. D. Durgin, "A 45 uW bias power, 34 dB gain reflection amplifier exploiting the tunneling effect for RFID applications," in *Proc. of the IEEE International Conference on RFID (RFID'2015)*, San Diego, CA, USA, Apr. 2015, pp. 137–144.

[10] J. Kimionis, A. Georgiadis, S. Kim, A. Collado, K. Niotaki, and M. M. Tentzeris, "An enhanced-range RFID tag using an ambient energy powered reflection amplifier," in *Proc. of the IEEE Int. Microwave Symp. (IMS'2014)*, Tampa, FL, USA, Jun. 2014, pp. 1–4.

[11] H. I. Cantu, V. F. Fusco, and S. Simms, "Microwave reflection amplifier for detection and tagging applications," *IET Microwaves, Antennas and Propagation*, vol. 2, no. 2, pp. 115–119, Mar. 2008.

[12] J. D. Griffin and G. D. Durgin, "Link envelope correlation in the backscatter channel," *IEEE Communications Letters*, vol. 11, no. 9, pp. 735–737, September 2007.

[13] ——, "Gains for RF tags using multiple antennas," *IEEE Transactions on Antennas and Propagation*, vol. 56, no. 2, pp. 563–570, Feb 2008.

[14] J. Kimionis, A. Bletsas, and J. N. Sahalos, "Increased range bistatic scatter radio," *IEEE Transactions on Communications*, vol. 62, no. 3, pp. 1091–1104, March 2014.

[15] P. N. Alevizos, A. Bletsas, and G. N. Karystinos, "Noncoherent short packet detection and decoding for scatter radio sensor networking," *IEEE Transactions on Communications*, vol. 65, no. 5, pp. 2128–2140, May 2017.

[16] W. Anran, I. Vikram, T. Vamsi, S. Joshua, and G. Shyamnath, "FM Backscatter: Enabling Connected Cities and Smart Fabrics," *NSDI 2017*, Feb 2017.

[17] C. Boyer and S. Roy, "Coded QAM backscatter modulation for RFID," *IEEE Transactions on Communications*, vol. 60, no. 7, pp. 1925–1934, Jul. 2012.

[18] ——, "Backscatter communication and RFID: Coding, energy, and MIMO analysis," *IEEE Transactions on Communications*, vol. 62, no. 3, pp. 770–785, March 2014.

[19] F. Farzami, S. Khaledian, B. Smida, and D. Erricolo, "Reconfigurable dual-band bidirectional reflection amplifier with applications in Van Atta array," *IEEE Transactions on Microwave Theory and Techniques*, no. 99, pp. 1–10, 2017.

[20] S. Khaledian, F. Farzami, D. Erricolo, and B. Smida, "A full-duplex bidirectional amplifier with low DC power consumption using tunnel diodes," *IEEE Microwave and Wireless Components Letters*, vol. 27, no. 12, pp. 1125–1127, Dec 2017.

[21] P. Chan and V. Fusco, "Full duplex reflection amplifier tag," *IET Microwaves, Antennas and Propagation*, vol. 7, no. 6, pp. 415–420, Apr. 2013.

[22] S. J. Chung, S. M. Chen, and Y. C. Lee, "A novel bi-directional amplifier with applications in active Van Atta retrodirective arrays," *IEEE Transactions on Microwave Theory and Techniques*, vol. 51, no. 2, pp. 542–547, Feb. 2003.

[23] M. Donelli, C. Saavedra, and M. Rukanuzzaman, "Design and Optimization of a Broadband X-Band Bidirectional Amplifier," *Microw. Opt. Technol. Lett*, vol. 55, no. 8, pp. 1730–1735, Aug. 2013.

[24] J. Van Bladel, "On the equivalent circuit of a receiving antenna," *IEEE Antennas and Propagation Magazine*, vol. 44, no. 1, pp. 164–165, Feb. 2002.

[25] F. Fuschini, C. Piersanti, F. Paolazzi, and G. Falciasecca, "Analytical approach to the backscattering from UHF RFID transponder," *IEEE Antennas and Wireless Propagation Letters*, vol. 7, pp. 33–35, Feb. 2008.

[26] S. R. Best and B. C. Kaanta, "A tutorial on the receiving and scattering properties of antennas," *IEEE Antennas and Propagation Magazine*, vol. 51, no. 5, pp. 26–37, Oct. 2009.

[27] R. C. Hansen, "Relationships between antennas as scatterers and as radiators," *Proceedings of the IEEE*, vol. 77, no. 5, pp. 659–662, May 1989.

[28] D. Bharadia, K. R. Joshi, M. Kotaru, and S. Katti, "BackFi: High throughput WiFi backscatter," in *Proc. of the 2015 ACM Conference on Special Interest Group on Data Communication*. ACM, 2015, pp. 283–296.

[29] A. Bletsas, A. G. Dimitriou, and J. N. Sahalos, "Improving backscatter radio tag efficiency," *IEEE Transactions on Microwave Theory and Techniques*, vol. 58, no. 6, pp. 1502–1509, Jun. 2010.

[30] N. Kingsley and J. R. Guerci, *Radar RF Circuit Design*. Artech House, 2016.

[31] A. S. A. Bechteler and T. F. Bechteler, "Switchless bidirectional amplifier for wireless communication systems," *Microw. Opt. Technol. Lett*, vol. 49, no. 8, pp. 1888–1890, May 2007.

[32] S. H. Weng, H. Y. Chang, and Y. C. Wang, "A broadband bidirectional amplifier using Gm- bandwidth extension technique," *IEEE Microw. Wirel. Compon. Lett*, vol. 26, no. 6, pp. 449–451, Jun. 2016.

[33] C. S. Yu, K. T. Mok, W. S. Chan, and S. W. Leung, "Switchless bidirectional amplifier," in *Proc. of the Asia-Pacific Microwave Conference (APMC'2006)*, Yokohama, Japan, Dec. 2006, pp. 476–479.

[34] J. F. Bousquet, S. Magierowski, and G. G. Messier, "A 4 GHz active scatterer in 130 nm CMOS for phase sweep amplify-and-forward," *IEEE Transactions on Circuits and Systems I: Regular Papers*, vol. 59, no. 3, pp. 529–540, Mar. 2012.

[35] D. Kim, M. A. Ingram, and W. W. Smith, "Measurements of small-scale fading and path loss for long range RF tags," *IEEE Transactions on Antennas and Propagation*, vol. 51, no. 8, pp. 1740–1749, Aug. 2003.

[36] J. D. Griffin and G. D. Durgin, "Multipath fading measurements at 5.8 GHz for backscatter tags with multiple antennas," *IEEE Transactions on Antennas and Propagation*, vol. 58, no. 11, pp. 3693–3700, Nov. 2010.

[37] F. J. Lopez-Martinez, L. Moreno-Pozas, U. Fernandez-Plazaola, J. F. Paris, E. Martos-Naya, and J. M. Romero-Jerez, "A tractable line-of-sight product channel model: Application to wireless powered communications," in *2018 15th International Symposium on Wireless Communication Systems (ISWCS)*, Aug 2018, pp. 1–5.

[38] M. K. Simon and M. S. Alouini, *Digital Communication Over Fading Channels*, 1st ed. New York, USA: Wiley, 2005.

[39] N. O'Donoughue and J. M. F. Moura, "On the product of independent complex Gaussians," *IEEE Transactions on Signal Processing*, vol. 60, no. 3, pp. 1050–1063, Mar. 2012.

[40] M. Abramowitz and I. A. Stegun, *Handbook of Mathematical Functions with Formulas, Graphs, and Mathematical Tables*, ser. National Bureau of Standards Applied Mathematics Series. New York: Dover Publications, 1964.

[41] A. Kilbas and M. Saigo, *H-Transforms : Theory and Applications (Analytical Method and Special Function)*, 1st ed. CRC Press, 2004.

[42] A. P. Prudnikov, Y. A. Brychkov, and O. I. Marichev, *Integral and Series: Volume 3, More Special Functions*. CRC Press Inc., 1990.

[43] G. T. Munsterman, "Tunnel Diode, Microwave Amplifier," *APL Technical Digest*, 1965.

[44] F. Farzami, S. Khaledian, B. Smida, and D. Erricolo, "Ultra-low power reflection amplifier using tunnel diode for RFID applications," in *2017 IEEE International Symposium on Antennas and Propagation and USNC/URSI National Radio Science Meeting*, July 2017, pp. 2511–2512.

[45] D. Seetharam and R. Fletcher, "Battery Powered RFID," *SenseID 2007 1st ACM Workshop on Convergence of RFID and Wireless Sensor Networks and their Applications*, Nov. 2007.

Seiran Khaledian (S'11) received her B.S. degree in electrical engineering from Khaje Nasir University of Technology (KNTU) in 2010 and M.S degree in telecommunication engineering from Tarbiat Modares University in 2013, Tehran, Iran. She is currently a Ph.D. student at the University of Illinois at Chicago (UIC). She is a member of the Networks Information Communications and Engineering Systems Laboratory (NICEST) at the UIC. Her research interests are in realization of 5G wireless communication systems, including full-duplex communication systems, analog self-interference cancellation techniques and reconfigurable antenna and RF/microwave components.

Farhad Farzami (S'10) received the Ph. D. in Electrical and Computer Engineering from the University of Illinois at Chicago (UIC), Chicago, Illinois, USA in 2018. He joined the Andrew Electromagnetics Lab at UIC in 2014 where he was researching in field of active and passive front-end microwave circuits and antennas. His research projects included metamaterial based RF circuits for realizing uniaxial propagation media and antenna miniaturization by using ultra-thin magneto-dielectric substrates, backscatter communication for full-duplex and RFID applications, reflection amplifiers, analog self-interference cancellation circuits and reconfigurable antennas for software defined radio applications. He joined Motorola Mobility in Chicago in 2018, where he is working as a senior RF engineer on RF circuits of cellphone products and the next generation (5G) of cellular communication.

Hamza Soury (S'11, M'2017) was born in Gafsa, Tunisia. He received the Diplome d'Ingenieur (Engineering degree) from the Ecole Polytechnique de Tunisie, La Marsa, Tunisia, in 2010, M.Sc. degree, and Ph.D. degree in Electrical Engineering from King Abdullah University of Science and Technology (KAUST) in 2012 and 2016, respectively. He is currently a Post-Doctoral Fellow with the department of electrical and computer engineering, University of Illinois at Chicago, USA. His research interests include the analysis performance of wireless networked control system with application to civil engineering.

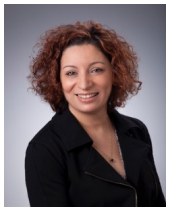

Besma Smida is an Associate Professor of Electrical and Computer Engineering at University of Illinois at Chicago. After completing her appointment as a Postdoc and later a Lecturer at Harvard University, she became an Assistant Professor of Electrical and Computer Engineering at Purdue University Calumet. Additionally, she was a Research Engineer in the Technology Evolution and Standards group of Microcell, Inc. (now Rogers Wireless), Montreal, Canada. Dr. Smida took part in wireless normalization committees (3GPP, T1P1). She obtained the Ph. D. and M. Sc. from the University of Quebec (INRS), Montreal, Canada. She is an associate Editor for the IEEE Communication letters and member of the IEEE ComSoc Emerging Technologies Committee. She was awarded the INSIGHT Into Diversity Magazine's 2015 "Inspiring Women in STEM". She received the Academic Gold Medal of the Governor General of Canada in 2007 and the NSF CAREER award in 2015. Her research focuses on wireless communication theory, full-duplex communication, radar, and backscatter modulation.

Danilo Erricolo (S'97-M'99-SM'03-F'16) received the Laurea degree of Doctor (summa cum laude) in electronics engineering from the Politecnico di Milano, Milan, Italy, in 1993 and the Ph.D. degree in electrical engineering and computer science from the University of Illinois at Chicago (UIC), Chicago, IL, USA, in 1998. He is a Professor in the Department of Electrical and Computer Engineering, the Director of the Andrew Electromagnetics Laboratory, and an adjunct Professor of Bioengineering at UIC. In 2017 he was nominated a University of Illinois Scholar. During the summer of 2009, he was an Air Force Faculty Fellow at the Air Force Research Laboratory, Wright-Patterson Air Force Base in Dayton, OH, USA. He has authored or coauthored more than 270 publications in refereed journals and international conferences. He has served as Associate Editor of the IEEE ANTENNAS AND WIRELESS PROPAGATION LETTERS (2002-2014), the IEEE TRANSACTIONS ON ANTENNAS AND PROPAGATION (2013-2016) and of Radio Science (2014-2016). In 2006, he was the Guest Editor of the special issues on RF effects on digital systems of the Electromagnetics Journal, and in 2012 he was the Lead Guest Editor of the special issue on Propagation models and inversion approaches for subsurface and through wall imaging, of the International Journal of Antennas and Propagation. His research interests are primarily in the areas of antenna design, electromagnetic propagation and scattering, high-frequency techniques, wireless communications, electromagnetic compatibility, the computation of special functions, and magnetic resonance imaging. Dr. Erricolo was elected Full Member of Commissions B, C and E of the U.S. National Committee (USNC) of the International Union of Radio Science (URSI), a committee of the US National Academies. He served as Chair (2009-2011), Vice Chair (2006-2008) and Secretary (2004-2005) of the USNC-URSI Commission E on Electromagnetic Environment and Interference. He was Chair of the USNC-URSI Ernest K. Smith Student Paper Competition (2009-2014); Vice-Chair of the Local Organizing Committee of the XXIX URSI General Assembly, held in Chicago, IL, USA in August 2008; and Member at Large of USNC-URSI (2012-2017). He served on the IEEE Antennas and Propagation Society (AP-S) Future Symposia Committee and on the IEEE AP-S/USNC-URSI Joint Meetings Committee (2006-2017 as a USNC-URSI representative). He was the General Chairman of the 2012 IEEE International Symposium on Antennas and Propagation and USNC-URSI National Radio Science Meeting, held in Chicago, IL, USA in July 2012. He was an Elected Member of the IEEE AP-S Administrative Committee (2012-2014); Chair of the IEEE AP-S Distinguished Lecturer Program (2015-2016); and Chair of the Chicago Joint Chapter of the IEEE AP-S and Microwave Theory and Techniques Society (2011-2016). He has served on more than 40 conference technical program committees, chaired over 60 conference sessions and organized more than 20 special sessions at international scientific conferences. He has been the Editor-in-Chief of the IEEE TRANSACTIONS ON ANTENNAS AND PROPAGATION since August 2016.